Optical bistability and self-opacity in magnetically doped monolayer transition metal dichalcogenides

Malcolm J. Regan [1], Yuriy G. Semenov,[1,2] and Ki Wook Kim [1,3,*]

[1] *Department of Electrical and Computer Engineering, North Carolina State University, Raleigh, North Carolina 27695, USA*

[2] *V. Lashkaryov Institute of Semiconductor Physics, National Academy of Science of Ukraine, Kyiv 03680, Ukraine*

[3] *Department of Physics, North Carolina State University, Raleigh, North Carolina 27695, USA*

(Received 22 September 2020; revised 27 November 2020; accepted 30 November 2020; published 22 December 2020)

Magneto-optical control of optical absorption spectra is theoretically investigated in two-dimensional (2D) dilute magnetic semiconductors such as monolayer transition metal dichalcogenides (TMDs) doped with magnetic ions. The underlying mechanism relies on efficient spin transfer between spin-polarized photoexcited carriers and localized magnetic ions via exchange scattering, and subsequent shifts in the electronic band structure induced by the resulting time-reversal symmetry breaking. A self-consistent model based on a rate equation is developed to analyze dynamical polarization of itinerant carrier spins and localized magnetic moments under circularly polarized optical excitation and the corresponding band modifications. The results illustrate that nonlinear effects such as optical bistability and self-opacity can indeed be achieved efficiently for a range of excitation power and frequency. In particular, the addition of magnetic dopants is shown to reduce the optical power required for the necessary band shifts by four orders of magnitude compared to that via the optical Stark effect in a nonmagnetic counterpart. Further investigation in a multidimensional parameter space elucidates the conditions for practical realization of the desired nonlinear effects in 2D TMD monolayers.

DOI: 10.1103/PhysRevB.102.214426

I. INTRODUCTION

Semiconducting monolayer (ML) transition metal dichalcogenides (TMDs) have recently received much attention for their potential use in a wide array of applications including electronic [1,2], photonic [3,4], and piezoelectric devices [5]. Further, ML TMDs have reinvigorated the field of valleytronics where the material's valley degree of freedom is employed to encode information [6,7]. Using the valley degree of freedom as a primary information carrier has the advantage of speed over charge-based devices. At the same time, it does not rely on the difficult-to-manage external fields required by many spin-based devices. These advantages offer unique opportunities to ML TMD-based valleytronics in both the classical [8] and quantum mechanical domains [9–15].

As it is well known, the motivation stems in large part from the ease with which lasting spin- and valley-polarized carrier populations can be generated selectively via optical excitation of a given helicity. The strong spin-orbital interaction characteristic to ML TMD crystals in combination with the broken inversion symmetry forces the bands in opposing K valleys of the hexagonal reciprocal lattice to spin split in contrast to one another. As optical transitions in K and K' (i.e., $-K$) valleys correspond to opposite angular momenta, light of opposite helicity selectively populates these bands [16]. Thus, the ability to manipulate their band structure via an external field is a topic of active interest. In particular, efforts to control optical absorption through Zeeman or Stark splitting of conduction and valence bands have been made for various ML TMDs. However, both theoretical and experimental investigations have revealed that extremely strong external fields are necessary to produce observable nonlinear effects [17–19]. This has motivated the efforts on approaches alternative to relying on external fields.

It has been shown that a pseudomagnetic field can be generated in a pristine ML TMD via the optical Stark effect induced by circularly polarized light [20,21]. However, observable modulation of the optical absorption requires extremely high-power laser pulses of the order 1×10^8 W/cm^2 (applied for very short periods of time $\sim$100 fs to protect samples from melting and destruction). The use of a magnetic exchange field was also examined theoretically in TMD MLs by exploiting the proximate interaction with an adjacent magnet [22]. A similar analysis on the optical Hall conductivity illustrated that a magnetic exchange field can dramatically enhance the magneto-optical response of TMDs without the use of large external magnetic fields [23]. The pronounced effect of this exchange mechanism was experimentally demonstrated in the spin-related valley splitting with the values two orders of magnitude larger than those achieved with an external field [24].

In this paper, we illustrate theoretically that ML TMDs doped with magnetic impurities can present an efficient route to significant nonlinear effects. The concept is grounded on the properties of the ML TMD band structure which facilitate polarization of localized spin moments (LSMs) of the magnetic dopants through exchange scattering with

*kwk@ncsu.edu

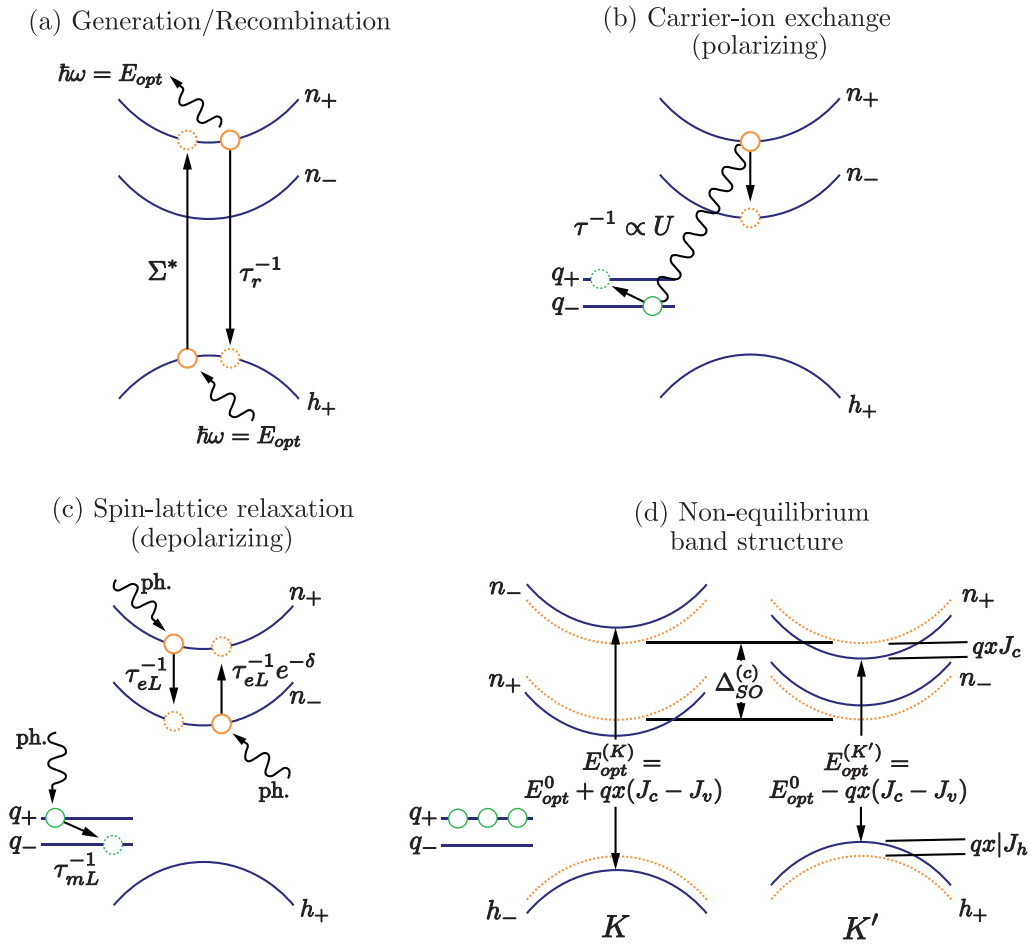

FIG. 1. Schematic illustrations of relevant processes annotated with symbols used. Subscripts of band labels denote only the direction of a carrier's spin (+, −) as the orbital contribution to the angular momentum is irrelevant to the carrier-ion exchange interaction. (a) Generation occurs across the optical band gap $E_{\rm opt}$ at a rate Σ^* from the uppermost valence subband h_- to the n_+ spin subband. Recombination occurs at a rate of τ_r^{-1}. (b) Carrier-ion exchange occurs between carriers in either subband and LSM of opposite spin at a rate proportional to universal parameter U [see Eqs. (9) and (11)]. As generation occurs only into the n_+ subband due to the selection rules, one expects a net LSM polarization $(q_+ - q_-)$, where q_+ and q_- are the populations of spin-up LSM and spin-down LSM, respectively. (c) Spin relaxation (i.e., spin-flip) due to the interaction with the lattice (i.e., phonons) occurs at a rate of τ_{eL}^{-1} for n_+ electrons, $\tau_{eL}^{-1}e^{-\delta}$ for n_- electrons, and τ_{mL}^{-1} for LSM. (d) Nonequilibrium band structures with narrowed $E_{\rm opt}^{(K')}$ and widened $E_{\rm opt}^{(K)}$ due to net LSM polarization x [$= (q_+ - q_-)/q$, where q is the total LSM population]. J_c (>0) and J_v (<0) are electron- and hole-exchange energies, respectively, $\Delta_{\rm SO}^{(c)}$ is the equilibrium spin-orbit splitting of the conduction subbands, and $E_{\rm opt}^0$ is the equilibrium optical band gap.

spin-polarized photocarriers [Figs. 1(a), 1(b), and 1(c)]. The time-reversal symmetry breaking induced by LSM polarization results in an exchange field which shifts the edges of the conduction and valence bands, drastically altering the fundamental absorption of the material [Fig. 1(d)]. Moreover, the carrier generation rate depends on optical absorption, which in itself depends on photoexcitation of the carriers (and subsequent shifts in the bands), presenting a nonlinearity favorable for realizing bistability of the optical absorption.

In what follows, the model describing the steady-state band carrier and LSM polarization in a dilute magnetic semiconducting ML TMD under circularly polarized optical excitation is developed. The numerical analysis of this model illustrates the parameter space in which the desired self-opacity and bistability effects can be realized and optically controlled.

II. THEORETICAL MODEL

A. Single-valley approximation

The ultimate goal of the following calculations is to find the conditions for dynamic spin polarization of dopant magnetic ions subjected to exchange scattering with photoexcited carriers as well as spin relaxation. The photocarriers transfer their nonequilibrium spin states through several channels such as nonradiative spin flip-flop scattering on the magnetic ions, spin relaxation via phonons, and (radiative and nonradiative) processes shortening their lifetimes. Further, intervalley transitions establish a distribution of conduction electrons and valence holes over K and K' valleys which could be an additional non-negligible factor affecting the LSM polarization.

In modeling the processes outlined above, a simple band structure consisting of two lowest conduction spin subbands and one highest valence spin subband in each valley is

sufficient to capture the salient features of the physical phenomenon under investigation. The spin splitting of the valence band is large enough that intravalley hole spin relaxation (thus, the second highest spin subband) can be ignored even at room temperature. Figure 1 illustrates the energy band structure subjected to the effective field of spin-polarized magnetic ions. The combination of the exchange field and the spin-orbital field induces band shifts in the opposite directions for the different valleys.

The overall state of the system is set by photoelectron and photohole populations $n_{\gamma,\sigma}$, h_γ ($\gamma = K, K'$; σ denoting spin subbands), and LSM distribution q_m over $2S+1$ spin states, where S is the total electronic spin of the magnetic dopants with a fixed concentration q ($= \sum_{m=-S}^{S} q_m$). Nonequilibrium states are controlled by the transition rates of electrons $\{\gamma,\sigma\} \longleftrightarrow \{\gamma',\sigma'\}$, holes $\{\gamma\} \longleftrightarrow \{\gamma'\}$, and LSM states $\{m\} \longleftrightarrow \{m'\}$. States further depend on electron-hole recombination and generation rates which themselves are a function of LSM polarization. The corresponding master equation describing these nonequilibrium processes includes too many unknown parameters, rendering a general form solution practically useless for further analysis. However, specific properties of the system allow for some simplifications to be made which enable analysis at a semiquantitative level.

The main idea is to develop a model which demonstrates the above-described nonlinear effects in the idealized case of a single valley (i.e., no intervalley scattering). The price for such a simplification is uncertainty in the value of relaxation parameters which are affected by intervalley transitions. However, the intervalley events involve large exchanges of carrier momenta (a significant fraction of the Brillouin zone width), which make their contribution to spin dynamics relatively small. Such qualitative speculations have robust experimental verification showing long spin relaxation times in nonmagnetic TMDs [25]. Further, the intervalley spin flip-flop transitions of electrons and holes polarize LSMs in the respectively opposite directions which may negate the net effect, at least in part. This single-valley approximation enables us to describe the desired nonlinear response in terms of a manageable number of parameters.

B. Exchange fields of localized spin moments

As indicated above, the carrier-ion exchange interaction plays a crucial role in the magneto-optical properties discussed here. This interaction is described by the Kondo Hamiltonian, which in quasimomentum representation for conduction ($b = c$) and valence ($b = v$) bands in a given valley (K or K') takes the form

$$H_{ex}^{(b)} = -\frac{1}{N_0}\sum_{j=1}^{N_m}\sum_{\sigma,\sigma',\mathbf{k},\mathbf{k}'} J_b e^{i(\mathbf{k}-\mathbf{k}')\cdot\mathbf{R}_j}\langle b,\sigma,\mathbf{k}|\mathbf{S}^j\cdot\mathbf{s}|b',\sigma',\mathbf{k}'\rangle \times a^\dagger_{b,\sigma,\mathbf{k}} a_{b',\sigma',\mathbf{k}'}, \quad (1)$$

where N_m and normalization factor N_0 account for the total number of LSM and TMD unit cells, respectively; J_b is the energy constant for the exchange interaction of electrons or holes with LSMs $\mathbf{S}^j$ situated at lattice sites $\mathbf{R}_j$; and $|b,\sigma,\mathbf{k}\rangle$ identifies the charge-carrier eigenstate in energy band b with wave vector $\mathbf{k}$ and spin state $\sigma = \pm 1$.

The electron/hole energy spectrum in the vicinity of a fixed valley γ of a pristine TMD ML can be written as

$$\varepsilon^{(b)}_{\gamma,\sigma,\mathbf{k}} = E_0^{(b)} + \frac{\hbar^2(\mathbf{k}-\gamma\mathbf{K})^2}{2m_b^*} + \frac{1}{2}\sigma\gamma\Delta_{\mathrm{SO}}^{(b)}, \quad (2)$$

where index $\gamma = \pm 1$ adapts for valleys K and K', m_b^* is the effective mass in the band b, and $E_0^{(b)} + \frac{1}{2}\sigma\gamma\Delta_{\mathrm{SO}}^{(b)}$ describes the minima of bands split in a spin-orbital field [26]. Because $\Delta_{\mathrm{SO}}^{(c)} \ll \Delta_{\mathrm{SO}}^{(v)}$, we focus on the optical transitions of electrons from the upper valence spin subband to the conduction subband that accommodates electrons of the same spin as illustrated in Fig. 1(a). With the time-reversal symmetry imposing that the product $\sigma\gamma$ be invariant for equal energy levels, the optical band gap at K and K' becomes $E_{\mathrm{opt}}^0 = E_0^{(c)} - E_0^{(v)} + \frac{1}{2}(\Delta_{\mathrm{SO}}^{(c)} - \Delta_{\mathrm{SO}}^{(v)})$ for the appropriate circular polarization of incident light.

The carrier-ion exchange interaction modifies the band gap via the diagonal part of the Hamiltonian [Eq. (1)]. In the mean-field approximation, the electron Zeeman energy $\frac{1}{2}\sigma G_b$ in the effective field

$$G_b = \frac{N_m}{N_0} J_b \langle S_z\rangle \quad (3)$$

causes a shift of the band gap, where $\langle S_z\rangle$ is the averaged LSM polarization. Thus, the final expression for the optical band gap of a magnetically doped ML TMD becomes

$$E_{\mathrm{opt}} = E_{\mathrm{opt}}^0 + \tfrac{1}{2}\sigma(G_c - G_v), \quad (4)$$

which shows the narrowing of E_{opt} in one valley and the widening of it in the other given that the spin subbands of the two valleys are reversals of each other.

The LSM polarization discussed here is mediated by photocarriers generated by absorption of monochromatic light with frequency ω. The rate of electron-hole generation Σ^* (thus, the absorption spectrum α) is modeled as a broadened step function

$$\Sigma^* = \Sigma_0^*\alpha = \Sigma_0^*\frac{\alpha_p}{2}\left(\tanh\frac{h\nu - E_{\mathrm{opt}}}{\varkappa} + 1\right), \quad (5)$$

where α_p is the maximum absorption value and $\Sigma_0^* = P/E_{\mathrm{opt}}$ accounts for illumination power P. The smearing $\varkappa$ in the band gap is caused by electron scattering with phonons, impurities, and lattice defects. Equation (5) shows that variation of E_{opt} around a laser energy within the range of $\varkappa$ would change the density of photocarriers. The carriers with an updated density would then polarize the LSMs, altering E_{opt} according to Eqs. (4) and (3). This nonlinear effect can be evaluated and analyzed in terms of a simplified master equation describing carrier populations of spin subbands and LSM polarization.

C. Reduced master equation

Consider an electron population generated in the subband $\sigma = +1$ of a given valley, which scatters away from this subband through recombination with holes after time τ_r, and through spin-flip transitions $\sigma \leftrightarrow \sigma'$ having rates $W^e_{+,-}$ and $W^e_{-,+}$. These rates tend to establish equilibrium populations of

spin subbands so that $W^e_{-,+}/W^e_{+,-} = e^{-\delta}$. Here,

$$\delta = \frac{\Delta^{(c)}_{\rm SO} + G_c}{k_B T} \tag{6}$$

as the subband $\sigma = +1$ is separated from the lower-lying subband $\sigma' = -1$ in energy by $\Delta^{(c)}_{\rm SO} + G_c$ and $k_B T$ is the thermal energy. With these considerations, the electron populations $n_\pm$ of spin subbands $\sigma = \pm 1$ in the given valley can be described as

$$\begin{aligned} \frac{dn_+}{dt} &= -n_+(W^e_{+,-} + \tau_r^{-1}) + n_- W^e_{-,+} + \Sigma^*, \\ \frac{dn_-}{dt} &= -n_-(W^e_{-,+} + \tau_r^{-1}) + n_+ W^e_{+,-}. \end{aligned} \tag{7}$$

Here, $W^e_{\sigma,\sigma'}$ depends on spin-lattice relaxation and carrier-ion exchange scattering, about which some additional simplifications can be made. For instance, the arbitrary spin S of the magnetic ions can be set to $S = \frac{1}{2}$. Calculations considering spins $S > \frac{1}{2}$ could be done for particular magnetic ions with known spin Hamiltonian parameters in a low-symmetry structure. However, this would be overly precise in the context of the idealized and semiquantitative approach taken in this work. By fixing S to a single value (i.e., $\frac{1}{2}$), the nonequilibrium spin polarization can be evaluated in terms of populations q_+ and q_- of LSM levels as $\langle S_z \rangle = \frac{q_+ - q_-}{2(q_+ + q_-)}$. The expression for the corresponding effective field is given above in Eq. (3) [i.e., the diagonal part of Eq. (1)].

The off-diagonal part of Kondo Hamiltonian [Eq. (1)] describes electron-exchange scattering with magnetic ions, the probability of which can be found from the first Born approximation for valley γ as [27]

$$W^{ex}_{\sigma,\sigma'} = q_{\sigma'} \frac{m_c^*(J_c A)^2}{\hbar^3} \min\left\{ \exp\left(\frac{\sigma - \sigma'}{2} \frac{\gamma \Delta^{(c)}_{\rm SO} + G_c}{kT} \right), 1 \right\}, \tag{8}$$

where A is the size (area) of the unit cell. In contrast, electron spin-lattice relaxation provides a channel for spin depolarization that countervails the influence of exchange scattering. Since the spin-lattice relaxation rate is quite specific to each particular magnetic TMD, it is treated here as an adjustable phenomenological parameter τ_{eL}^{-1}. As stated above, the electron kinetics involve both spin-flip transitions:

$$\begin{aligned} W^e_{+,-} &= q_- U + \tau_{eL}^{-1}, \\ W^e_{-,+} &= q_+ U e^{-\delta} + \tau_{eL}^{-1} e^{-\delta}, \end{aligned} \tag{9}$$

where $U = m_c^*(J_c A)^2/\hbar^3$. It is useful to note that carrier-ion exchange depends on the LSM populations $q_\pm$ while spin-lattice relaxation does not.

Likewise, the LSM populations q_σ depend on the exchange scattering with the electrons and the depolarizing interaction with the lattice (i.e., phonons). The corresponding equations are similar to Eq. (7) if one takes into account that recombination and photogeneration are irrelevant for magnetic ions,

$$\begin{aligned} \frac{dq_+}{dt} &= q_- W^m_{-,+} - q_+ W^m_{+,-}, \\ \frac{dq_-}{dt} &= q_+ W^m_{+,-} - q_- W^m_{-,+}. \end{aligned} \tag{10}$$

Here, $W^m_{\sigma,\sigma'}$ is the rate at which magnetic ions undergo spin flips from the state with $S_z = \frac{1}{2}\sigma$ to that with $S_z = \frac{1}{2}\sigma'$. The formal expressions for the rates of such transitions can also be written just like those for the carrier spins [i.e., Eq. (9)],

$$\begin{aligned} W^m_{+,-} &= n_- U e^{-\delta} + \tau_{mL}^{-1}, \\ W^m_{-,+} &= n_+ U + \tau_{mL}^{-1}, \end{aligned} \tag{11}$$

where the spin-lattice relaxation rate τ_{mL}^{-1} (for the magnetic ions) is taken to be the same for the processes in both directions (+, − and −, +) as the splitting between the LSM levels is assumed to be small compared to $k_B T$.

Setting the time derivatives of Eqs. (7) and (10) to zero transforms them into algebraic equations describing the stationary states. It is convenient to represent these equations in terms of the normalized conduction electron polarization $y = \frac{n_+ - n_-}{n}$ and LSM polarization $x = \frac{q_+ - q_-}{q}$ as

$$y = \frac{x - y_0 + \left[\tau_r^{-1} - y_0 \tau_{eL}^{-1}(1 + e^{-\delta})\right]/\tau_{eM}^{-1}}{1 - x y_0 + \tau_{eLr}^{-1}/\tau_{eM}^{-1}}, \tag{12}$$

$$x = \frac{nU(1 + e^{-\delta})(y + y_0)}{nU(1 + e^{-\delta})(1 + y y_0) + 4\tau_{mL}^{-1}}. \tag{13}$$

In these expressions, the optical power and recombination time control the total electron population $n = n_+ + n_- = \tau_r \Sigma^*$, $y_0 = \tanh(\frac{\delta}{2})$ corresponds to the equilibrium populations of spin-split subbands, $\tau_{eM}^{-1} = \frac{1}{2} q U (1 + e^{-\delta})$ is a rate of exchange scattering, and $\tau_{eLr}^{-1} = \tau_r^{-1} + \tau_{eL}^{-1}(1 + e^{-\delta})$ describes the rate of spin depolarization via recombination and spin-lattice relaxation.

Equation (13) clearly shows an absence of any LSM polarization without optical pumping (i.e., $n = 0$); it also indicates saturated LSM polarization $x \to 1$ when exchange scattering prevails over lattice relaxation at stronger optical pumping. The actual situation is much more complicated if one takes into account the nonlinear dependence of photogeneration $n = \tau_r \Sigma^*$ [Eq. (5)] on the LSM polarization. The numerical solutions of these equations are discussed in the next section.

III. RESULTS AND DISCUSSION

The parameter values listed in Table I are used unless stated otherwise. Where available, values in the neighborhood of those experimentally observed for WS_2 are selected. Solutions for LSM polarization from Eq. (13) and at varying optical powers and frequencies yield steady-state absorption spectra per Eq. (5) as shown in Fig. 2. As the power of the excitation changes, the absorption characteristics at/around the excitation frequency shift. Specifically, the spectrum appears to lean over with power toward the low-frequency side below $E^0_{\rm opt}$. In fact, the material becomes more opaque in this spectral region due to the increased absorption (see the block arrow in Fig. 2). The band-gap narrowing caused by the LSM polarization is apparent from the results. At higher powers, some frequencies yield multiple solutions, indicating optical bistability. For instance, the 40-kW/cm^2 curve (Fig. 2) experiences sudden transitions to high- and low-absorption states marked by two arrowed lines around $\hbar\omega - E^0_{\rm opt} = 25$ meV as the excitation frequency sweeps. The width of the hysteretic region is approximately 10 meV, in which the dotted curve

TABLE I. Numerical values of the parameters used in the calculation. m_0 denotes the electron rest mass.

E^0_{opt}	$\Delta^{(c)}_{\text{SO}}$	α_p	τ_r	τ_{eL}	τ_{mL}	J_c	J_v	m^*_c	q
2.8 eV	41 meV	0.09	50 ps	100 ps	300 ps	0.5 eV	−1 eV	$0.5m_0$	6.25%

corresponds to unstable solutions. In the following discussion, the model is analyzed to determine the parameter space where one can expect to realistically observe the changes to material transparency or opacity and the optical bistability predicted by the model.

A. Self-opacity

At frequencies within the range of $\varkappa$ (band smearing) from the optical band gap where the photogeneration rates can be readily induced, relatively modest optical excitation power can cause significant changes in the optical absorption. The calculated change $\Delta\alpha$ from initial- to steady-state absorption is plotted in Fig. 3(a) across excitation frequency for varying power. The strength of this effect is dependent on model parameters. One of the most significant dependencies is the slope of the material's absorption spectrum about E^0_{opt}, set by $\varkappa$. This is illustrated in Fig. 3(b) where it can be seen that large changes in absorption are more easily produced on spectra featuring abrupt transitions from low to high absorption. Further, shorter recombination time, longer relaxation times, and larger exchange constants result in more pronounced changes in absorption with respect to the parameter values of Table I. The fact that faster recombination could result in more pronounced nonlinear effects is surprising given that one would expect carrier recombination to act as a drain on the power which primarily drives the realization of these effects. This result is discussed in greater detail in the context of optical bistability in Sec. III B.

It is interesting to note that spectral shifts of an exciton absorption peak comparable to the changes shown in Fig. 3 were experimentally reported in pristine ML WS_2 via the optical Stark effect using a pulse of 0.24 GW/cm^2 [20]. While a direct comparison between these two cases is not possible due to their differences (e.g., exciton vs band-edge transitions), the four orders of magnitude reduction in power seen here suggests that magnetic TMDs have an exceedingly efficient nonlinear response. The physical mechanism responsible for the optical Stark effect under very strong illumination is also much different from and thus cannot be described by the model discussed in this work.

B. Optical bistability

At higher-power excitations at the edge of the band gap, optical bistability can be induced as illustrated in Fig. 2. This effect has parameter dependencies similar to those of the self-opacity discussed above. Particularly, the power and frequency of an excitation able to cause optical bistability has a strong dependence on the parameter $\varkappa$, as shown in Fig. 4. With a larger $\varkappa$, the transition between low and high absorption values of the initial spectrum becomes more gradual. Accordingly, higher powers are required for the bistability and the contrast between stable states (i.e., the difference between the high and low absorption α_H and α_L) degrades along with a narrower spectral window. Moreover, the tip of the bistable region moves further away from the band-gap edge, rendering bistability even more difficult to realize. By contrast, larger exchange energies improve bistability conditions as expected (Fig. 5). Evidently, this shows the ability to polarize the LSMs efficiently with the incident light, where the spin-polarized photo-carriers provide the intermediary.

As discussed briefly above, the recombination time τ_r manifests a nontrivial influence on the bistability. Unexpectedly, longer electron lifetimes tend to diminish the bistability effect as can be seen from Fig. 6(a). It appears that the net polarization of the photoexcited carrier spins is enhanced with a shorter τ_r [see Eq. (12)] since this process effectively competes with and thus partly neutralizes the detrimental effect

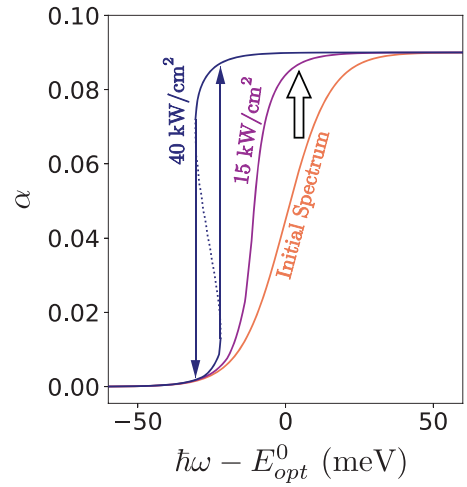

FIG. 2. Steady-state absorption spectra at varying powers with $\varkappa = 15$ meV. The dotted curve represents unstable solutions, while the solid arrows indicate the hysteresis loop for optical bistability.

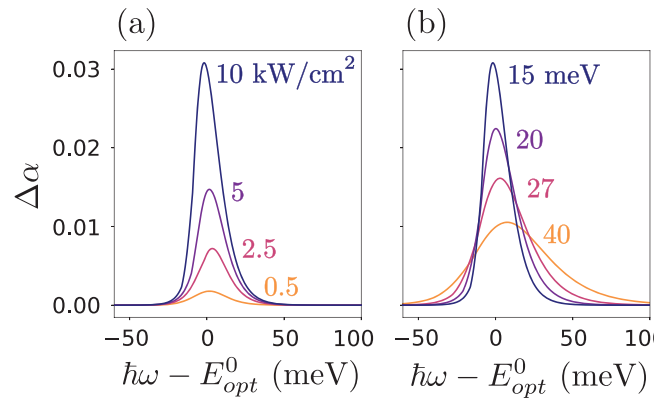

FIG. 3. Change in the absorption induced by the nonlinear effect as a function of incident photon energy with (a) varying power at $\varkappa = 15$ meV and (b) varying $\varkappa$ at a power of 10 kW/cm^2.

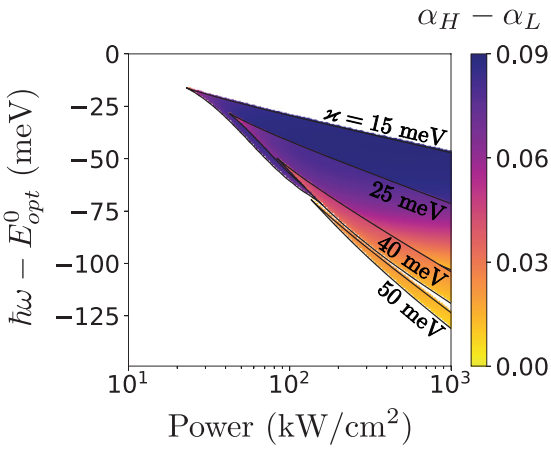

FIG. 4. Frequency-power regions of optical bistability for varying $\varkappa$. The color map indicates contrast between the two stable states (i.e., the difference between the high and low absorption α_H and α_L).

of spin-lattice relaxation τ_{eL}. Further, despite the reduction in the total electron population n $(= n_+ + n_-)$, the direct impact of the recombination itself on the net polarization $n_+ - n_-$ becomes rather muted as τ_r affects both n_+ and n_- equally. Hence, a shorter τ_r, particularly in reference to τ_{eL}, may be more favorable. However, once τ_r becomes too short to support a sufficient photocarrier density [i.e., $\tau_r \ll 1/(\Sigma^* U \tau_{mL})$], the rate of LSM polarization in Eq. (11) is dominated by the relaxation term τ_{mL}^{-1}, rendering the high-absorption state (thus, the optical bistability) unsustainable. This can be seen from Fig. 7, where the upper branch of the normalized LSM polarization x (i.e., the high-absorption state) ceases to exist around $\tau_r = 0.1$ ps (i.e., no bistability).

As for τ_{eL} and τ_{mL}, shorter relaxation times clearly suppress the possibility of two stable states at the same optical conditions [Figs. 6(b) and 6(c)]. In particular, the impact of τ_{eL} on the bistability appears to be felt most sensitively when the characteristic time approaches that of recombination (e.g., 50 ps), but becomes far more gradual past this point, consistent

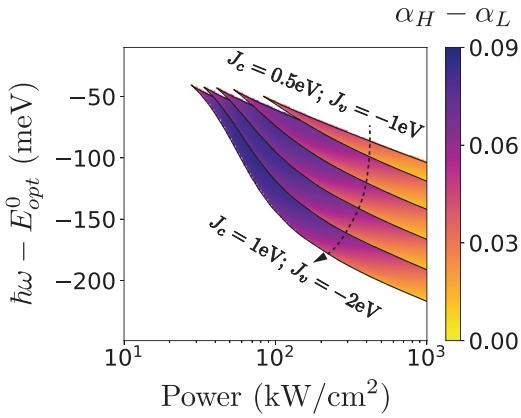

FIG. 5. Frequency-power regions of optical bistability for varying exchange energies at $\varkappa = 40$ meV. Exchange energies used, from top to bottom, in units of eV are $J_c, J_v = 0.5, -1; 0.625, -1.25; 0.75, -1.5; 0.875, -1.75; 1, -2$. The color map indicates contrast between the two stable states as in Fig. 4.

with observations of the rightmost boundary of the upper branch in Fig. 7. Note that the value of τ_{eL} does not act as a hard limit on the value of τ_r necessary for bistability to occur. The seeming cutoff at $\tau_r = \tau_{eL}$ in Fig. 7 is actually coincidental to the specific choice of excitation frequency and power. This is evident from the analysis shown in Figs. 6(a) and 6(b) for a broader parameter space. It clearly illustrates the existence of bistability window even when $\tau_r > \tau_{eL}$. Nevertheless, τ_{eL} provides a good indicator for the value of τ_r necessary for the robust appearance of bistability.

C. Effect of intervalley scattering on the single-valley model

Including the consideration of carriers in the second valley whose band populations are controlled by the spin-conserving intervalley transitions (W_{iv}) increases the number of terms in Eq. (7), causing the model to become too complicated for a general analysis. However, one can consider an effective description in which the loss of carriers to the second valley is incorporated into through a modified recombination rate $\tau_{r^*}^{-1}$ in a single-valley treatment. Likewise, $\tau_{mL^*}^{-1}$ and $\tau_{eL^*}^{-1}$ can be adopted to account for the modified spin-lattice relaxation rates for magnetic ions (i.e., LSM polarization) and electrons.

The two-valley solution yields spin subband populations $n_{1,+}, n_{1,-}, n_{2,+}, n_{2,-}$ which can be used to calculate the effective rates. For instance, the decreased electron population n_1 $(= n_{1,+} + n_{1,-})$ in the valley of interest can be accounted for by proportionately increasing the effective recombination rate in the one-valley model. While the rate of electron-hole generation rate Σ^* remains unchanged as given in Eq. (5), some of the excited electrons are now transferred to the second valley, reducing n_1 $(< n)$. Considering the relation $\tau_r^{-1} = \Sigma^*/n$ defined earlier, the modified recombination rate can be written as $\tau_{r^*}^{-1} = \Sigma^*/n_1$ leading to

$$\frac{\tau_{r^*}^{-1}}{\tau_r^{-1}} = \frac{n}{n_1}. \tag{14}$$

Further, the effective single-valley spin-lattice relaxation rate for the magnetic ions can be found by solving Eqs. (11) and (10) with $n_{1,+}$ and $n_{1,-}$ instead,

$$\tau_{mL^*}^{-1} = U e^{-\delta_1} \frac{q_- n_{1,+} - q_+ n_{1,-}}{q_+ - q_-}. \tag{15}$$

Actually, it can be verified that this quantity describes a τ_{mL}^{-1} altered by the net exchange scattering with the second-valley carriers. By extending Eqs. (11) and (10) to include the contribution of these additional processes, one can arrive at the solution

$$\begin{aligned} \tau_{mL^*}^{-1} &= U e^{-\delta_1} \frac{q_- n_{1,+} - q_+ n_{1,-}}{q_+ - q_-} \\ &= \tau_{mL}^{-1} + U e^{-\delta_2} \frac{q_+ n_{2,-} - q_- n_{2,+}}{q_+ - q_-} \end{aligned} \tag{16}$$

or

$$\frac{\tau_{mL^*}^{-1}}{\tau_{mL}^{-1}} = \frac{e^{-\delta_1}(q_- n_{1,+} - q_+ n_{1,-})}{e^{-\delta_1}(q_- n_{1,+} - q_+ n_{1,-}) + e^{-\delta_2}(q_- n_{2,+} - q_+ n_{2,-})}. \tag{17}$$

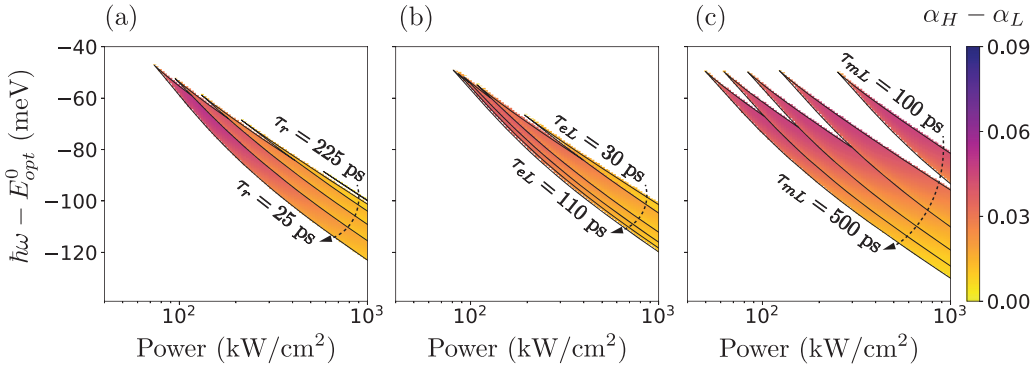

FIG. 6. Frequency-power regions of optical bistability for varying recombination and relaxation times at $\varkappa = 40$ meV. The color map indicates contrast between the two stable states as in Fig. 4. In (a)–(c), τ_r, τ_{eL}, and τ_{mL} vary in steps of 50, 20, and 100 ps, respectively.

Finally, having calculated $\frac{\tau_{r*}^{-1}}{\tau_r^{-1}}$ and $\frac{\tau_{mL*}^{-1}}{\tau_{mL}^{-1}}$, the last parameter $\frac{\tau_{eL*}^{-1}}{\tau_{eL}^{-1}}$ can be found by matching the effective single-valley calculation with the corresponding two-valley result. These effective rates are generally functions of power, frequency, and other physical variables.

In a fitting done for the parameter set of Table I, the effective rates are found to have dependence on $\log_{10} W_{iv}$ with the form of either hyperbolic tangent (τ_{r*}^{-1}) or sigmoid (τ_{eL*}^{-1}, τ_{mL*}^{-1}) functions. As valley decoherence time has been measured to be in the hundreds of fs [9], these effective relaxation rates would be near their asymptotic values under most normal conditions. As such, they likely do not need to be cast as functions of W_{iv}. Accordingly, it is expected that the one-valley model can effectively emulate the dynamics in ML TMDs with K and K' valleys.

IV. SUMMARY

A model for self-consistent LSM polarization and associated nonlinear effects is developed in dilute magnetic ML TMDs under circularly polarized optical excitation. Numerical evaluation of the model suggests that magneto-optically induced changes to absorption of a magnetically doped TMD ML are possible at powers orders of magnitude lower than those required for comparable changes in pristine ML TMDs. The results also predict that significant changes to absorption are possible over a wide range of realistic material parameters. The strength of the predicted absorption modulation effect becomes more pronounced with smaller band smearing, shorter recombination time (but not too short), larger exchange energies, and longer relaxation times.

Compared to the self-opacity/transparency phenomenon, the optical bistability predicted at higher powers is more sensitive to parameter values. Further, the band of frequencies at which it can be realistically induced is more restricted. In particular, optical bistability is predicted to occur mostly at photon energies far from the absorption edge where only a very small density of photocarriers can be excited without the band modification induced by LSM polarization. The conditions for bistability occurring at these frequencies, the level of optical power required, and the contrast between stable states improve with the same parameter trends that increase the strength of the absorption modulation effect. Consideration of higher-order terms such as Berry's curvature in these 2D chiral systems is outside the scope of the current investigation. Overall, ML TMDs doped with magnetic ions offer unique opportunities to realize the nonlinear optical effects at record-low optical power.

ACKNOWLEDGMENTS

This work was supported, in part, by the U. S. Army Research Office (Grant No. W911NF-16-1-0472).

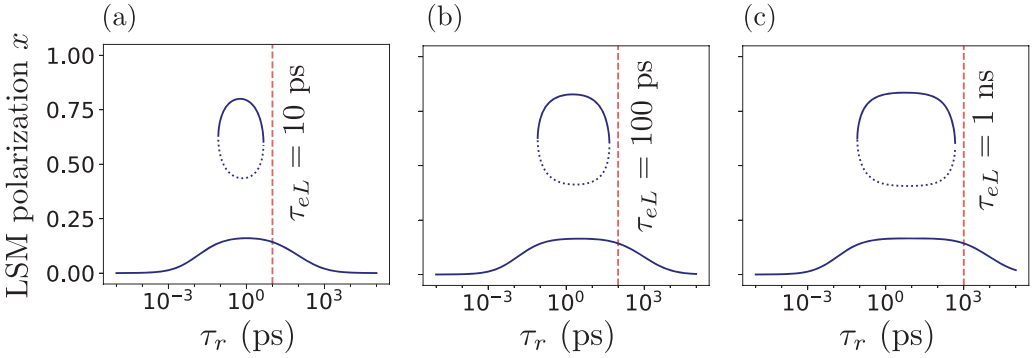

FIG. 7. LSM polarization vs recombination time with varying τ_{eL} at $\varkappa = 40$ meV, $\hbar\omega - E^0_{\rm opt} = -65$ meV, and optical power $P = 110$ kW/cm^2. The presence of two stable solutions (solid lines) at a given τ_r indicates the window of optical bistability. The deviation in x outside this region in the lower branch corresponds to self-opacity.

[1] B. Rawat, M. M. Vinaya, and R. Paily, Transition metal dichalcogenide-based field-effect transistors for analog/mixed-signal applications, IEEE Trans. Electron Devices **66**, 2424 (2019).

[2] T. Kim, D. Kang, Y. Lee, S. Hong, H. G. Shin, H. Bae, Y. Yi, K. Kim, and S. Im, 2D TMD channel transisters with ZnO nanowire gate for extended nonvolatile memory applications, Adv. Funct. Mater. **30**, 2004140 (2020).

[3] I. Datta, S. H. Chae, G. R. Bhatt, M. A. Tadayon, B. Li, Y. Yu, C. Park, J. Park, L. Cao, D. N. Basov, J. Hone, and M. Lipson, Low-loss composite photonic platform based on 2D semiconductor monolayers, Nat. Photonics **14**, 256 (2020).

[4] X. Zhang, X. Zhang, W. Huang, K. Wu, M. Zhao, A. T. C. Johnson, S. Tongay, and E. Cubukcu, Ultrathin WS_2-on-glass photonic crystal for self-resonant exciton-polaritonics, Adv. Opt. Mater. **8**, 1901988 (2020).

[5] J. Kim, E. Lee, S. Bhoyate, and T. K. An, Stable and high-performance piezoelectric sensor via CVD grown WS_2, Nanotechnol. **31**, 445203 (2020).

[6] X. Cu, W. Yao, D. Xiao, and T. Heinz, Spin and pseudospins in layered transition metal dichalcogenides, Nat. Phys. **10**, 343 (2014).

[7] Y. Liu, Y. Gao, S. Zhang, J. He, J. Yu, and Z. Liu, Valleytronics in transition metal dichalcogenides materials, Nano Res. **12**, 2695 (2019).

[8] L. Li, L. Shao, X. Liu, A. Gao, H. Wang, B. Zheng, G. Hou, K. Shehzad, L. Yu, F. Miao, Y. Shi, Y. Xu, and X. Wang, Room-temperature valleytronic transistor, Nat. Nanotechnol. **15**, 743 (2020).

[9] A. Kormányos, V. Zólyomi, N. D. Drummond, and G. Burkard, Spin-Orbit Coupling, Quantum Dots, and Qubits in Monolayer Transition Metal Dichalcogenides, Phys. Rev. X **4**, 011034 (2014).

[10] Z. Ye, D. Sun, and T. F. Heinz, Optical manipulation of valley pseudospin, Nat. Phys. **13**, 26 (2017).

[11] J. Pawłowski, Spin-valley system in a gated MoS_2-monolayer quantum dot, New J. Phys. **21**, 123029 (2019).

[12] J. Pawłowski, D. Żebrowski, and S. Bednarek, Valley qubit in a gated MoS_2 monolayer quantum dot, Phys. Rev. B **97**, 155412 (2018).

[13] Y. Wu, Q. Tong, G.-B. Liu, H. Yu, and W. Yao, Spin-valley qubit in nanostructures of monolayer semiconductors: Optical control and hyperfine interaction, Phys. Rev. B **93**, 045313 (2016).

[14] G. Széchenyi, L. Chirolli, and A. Pályi, Impurity-assisted electric control of spin-valley qubits in monolayer MoS_2, 2D Mater. **5**, 035004 (2018).

[15] M. Brooks and G. Burkard, Electric dipole spin resonance of two-dimensional semiconductor spin qubits, Phys. Rev. B **101**, 035204 (2020).

[16] D. Xiao, G.-B. Liu, W. Feng, X. Xu, and W. Yao, Coupled Spin and Valley Physics in Monolayers of MoS_2 and Other Group-VI Dichalcogenides, Phys. Rev. Lett. **108**, 196802 (2012).

[17] N. D. Hien, C. V. Nguyen, N. N. Hieu, S. S. Kubakaddi, C. A. Duque, M. E. Mora-Ramos, L. Dinh, T. N. Bich, and H. V. Phuc, Magneto-optical transport properties of monolayer transition metal dichalcogenides, Phys. Rev. B **101**, 045424 (2020).

[18] M. Tahir and P. Vasilopoulos, Magneto-optical transport properties of monolayer WSe_2, Phys. Rev. B **94**, 045415 (2016).

[19] C. V. Nguyen, N. N. Hieu, N. A. Poklonski, V. V. Ilyasov, L. Dinh, T. C. Phong, L. V. Tung, and H. V. Phuc, Magneto-optical transport properties of monolayer MoS_2 on polar substrates, Phys. Rev. B **96**, 125411 (2017).

[20] E. J. Sie, J. W. McIver, Y.-H. Lee, L. Fu, J. Kong, and N. Gedik, Valley-selective optical stark effect in monolayer WS_2, Nat. Mater. **14**, 290 (2015).

[21] J. Kim, X. Hong, C. Jin, S.-F. Shi, C.-Y. S. Chang, M.-H. Chiu, L.-J. Li, and F. Wang, Ultrafast generation of pseudo-magnetic field for valley excitons in WSe_2 monolayers, Science **346**, 1205 (2014).

[22] Y. G. Semenov and K. W. Kim, Bias driven spontaneous spin-valley polarization in monolayer transition-metal dichalcogenides, Phys. Rev. B **93**, 041414(R) (2016).

[23] H. Da, L. Gao, W. Ding, and X. Yan, Nonreciprocal giant magneto-optic effects in transition-metal dichalcogenides without magnetic field, J. Phys. Chem. Lett. **8**, 3805 (2017).

[24] T. Norden, C. Zhao, P. Zhang, R. Sabirianov, A. Petrou, and H. Zeng, Giant valley splitting in monolayer WS_2 by magnetic proximity effect, Nat. Commun. **10**, 4163 (2019).

[25] L. Yang, N. A. Sinitsyn, W. Chen, J. Yuan, J. Zhang, J. Lou, and S. A. Crooker, Long-lined nanosecond spin relaxation and spin coherence of electrons in monolayer MoS_2 and WS_2, Nat. Phys. **11**, 830 (2015).

[26] H. Rostami, A. G. Moghaddam, and R. Asgari, Effective lattice Hamiltonian for monolayer MoS_2: Tailoring electronic structure with perpendicular electric and magnetic fields, Phys. Rev. B **88**, 085440 (2013).

[27] Y. G. Semenov, Electron spin relaxation in semiconductors and semiconductor structures, Phys. Rev. B **67**, 115319 (2003).